Comparison of stress dependent geophysical, hydraulic and mechanical properties of synthetic and natural sandstones for reservoir characterisation and monitoring studies

by

Ismael Himar Falcon-Suarez[1*]
Kelvin Amalokwu[2]
Jordi Delgado-Martin[3]
Ben Callow[4]
Katleen Robert[1]
Laurence North[1]
Sourav K. Sahoo[4]
&
Angus I. Best[1]

(1) National Oceanography Centre, University of Southampton Waterfront Campus. European Way, SO14 3ZH, Southampton, United Kingdom.

(2) The University of Texas at Austin, Jackson School of Geosciences, Austin, Texas, USA.

(3) Civil Engineering School. University of A Coruña. Campus de Elviña s/n. 15192 A Coruña. Spain.

(4) University of Southampton, Ocean and Earth Science, Southampton, SO14 3ZH, United Kingdom.

Submitted to:

GP Special issue "*Rock-physics - From microstructure to seismic signatures*"

[*]Corresponding author: National Oceanography Centre, University of Southampton Waterfront Campus. European Way, SO14 3ZH, Southampton, UK.

Phone: +44 (0)23 8059 6666 Office: 786/24 email: isfalc@noc.ac.uk

Abstract

Synthetic rock samples can offer advantages over natural rock samples when used for laboratory rock physical properties studies, provided their success as natural analogues is well understood. The ability of synthetic rocks to mimic the natural stress dependency of elastic wave, electrical and fluid transport properties is of primary interest. Hence, we compare a consistent set of laboratory multi-physics measurements obtained on four quartz sandstone samples (porosity range 20 – 25%) comprising two synthetic and two natural (Berea and Corvio) samples, the latter used extensively as standards in rock physics research. We measured simultaneously ultrasonic (P and S-wave) velocity and attenuation, electrical resistivity, permeability, and axial and radial strains over a wide range of differential pressure (confining stress 15 - 50 MPa; pore pressure 5 - 10 MPa), on the four brine saturated samples. Despite some obvious physical discrepancies caused by the synthetic manufacturing process, such as silica cementation and anisotropy, the results show only small differences in stress dependency between the synthetic and natural sandstones for all measured parameters. Stress-dependency analysis of the dry samples using an isotropic effective medium model of spheroidal pores and penny-shaped cracks, together with a granular cohesion model, provide evidence of crack closure mechanisms in the natural sandstones, seen to a much lesser extent in the synthetic sandstones. The smaller grain size, greater cement content, and cementation under oedometric conditions particularly affect the fluid transport properties of the synthetic sandstones, resulting in lower permeability and higher electrical resistivity for a similar porosity. The effective stress coefficients, determined for each parameter, are in agreement with data reported in the literature. Our results for the particular synthetic materials that were tested suggest that

synthetic sandstones can serve as good proxies for natural sandstones for studies of elastic and mechanical properties, but should be used with care for transport properties studies.

Key words: Elastics, resistivity, permeability, strains, effective stress.

1. Introduction

The availability of reservoir samples is challenging, since it commonly depends on direct agreements with the private sector (e.g., oil and gas companies). When available, natural samples may present some alteration due to the recovery processes, such as drilling, coring and grinding. These processes affect the preservation of the original geomechanical properties of the rock formation, resulting from stress-release induced-microcracks generation (Holt et al. 2000). The induced damage is particularly concerning in soft rocks, such as weakly cemented sandstones (Li and Fjær 2012), of great interest for oil and gas industry (i.e., widely extended hydrocarbon reservoir formations).

Synthetic sandstones appear as interesting alternatives to natural sandstones either as substitutes when reservoir sandstones are not available, or in cases where certain controlled composition and/or inclusion geometry is required (e.g., Amalokwu et al. 2016, Amalokwu et al. 2015a). They allow replication of compositionally realistic reservoir formations, as well as control of porosity and strength. However, it has been posed that the manufactured samples may unrealistically imitate some properties of their natural analogues, particularly those related to grain-to-grain contacts (Bernabé et al. 1992). The celerity of the synthetic samples manufacturing process is orders of magnitude faster than those of natural sandstones generation environments, where free gravity-driven grain deposition, diagenesis and long-term compaction characterise the resulting rock formation.

Genetic environment constrains grain orientation and packing, degree of compaction and cementation. Grain assembly affects the cohesion and friction between particles, and the inhomogeneity of the stress-induced strains. In sands, grain sizes, stress history during burial and initial porosity particularly influence the

flow properties of the resulting sandstone (Brzesowsky et al. 2014). The effect that these differences between synthetic and natural rocks have on their corresponding elastic, mechanical and transport properties is still unclear. Furthermore, these properties are also pressure-dependent and variably affected by the confining and pore pressures (Berryman 1992). Such dependencies can be studied through the effective stress coefficient concept, using any measured property of the material (Todd and Simmons 1972).

In the last decades, there have been a number of experiments performed with synthetic sandstones in the field of rock physics, studying pressure-dependence, pore fluid and anisotropy of elastic properties. From them, the use of synthetic sandstones appeared as a suitable alternative to isolate the individual contributions of the different elements of rock matrix, with counteracting effects. Bernabé et al. (1992), den Brok et al. (1997) and David et al. (1998) studied the cementation effect in rock strength using silica-cemented synthetic sandstones. Holt et al. (2005) and Holt and Stenebråten (2013) investigated the effect of pore pressure and saturation on the stress-dependency of anisotropic wave velocities using synthetic sandstones. Rathore et al. (1995) studied the anisotropy of P and S-waves in dry and saturated epoxy-cemented sand, with metallic discs chemically removed to leave crack-like shapes in the matrix. This manufacturing technique was later adapted by Tillotson et al. (2011) and Tillotson et al. (2012) to create silica cemented sandstone samples with aligned fractures to investigate relations between S-wave splitting, fracture density and pore fluid composition. Applying Tillotson's technique, Amalokwu et al. (2014) studied partial water saturation in oriented aligned fracture synthetic silica cemented sandstones. Amalokwu et al. (2015a) and Amalokwu et al. (2015b) extended the study of P-wave anisotropy and S-wave splitting to oblique angles

oriented fracture synthetic sandstone samples, while Amalokwu et al. (2016) investigated the effect of aligned fractures on V_p/V_s and Q_s/Q_p ratios.

Synthetic samples have also been used to study transport mechanisms in porous media. For instance, Crawford et al. (2008) elaborated aggregates of quartz and kaolinite at variable ratios to investigate the frictional strength and permeability of fault zones, and the influence of clay content in both parameters. More recently, Falcon-Suarez et al. (2016) and Falcon-Suarez et al. (2017b) used silica cement synthetic sandstone to investigate pore fluid distribution and pore pressure-induced geomechanical effects during CO_2 geosequestration in siliciclastic shallow saline reservoirs.

In this work, we study the extent to which natural and synthetic sandstones are comparable, by analysing the effect that confining stress and pore pressure have on their physical, mechanical and hydraulic properties. Ultrasonic wave propagation, volumetric deformation, electrical resistivity and permeability changes are measured for a defined differential pressure path in four core samples: two natural sandstones and two synthetics of similar mineralogy and porosity. This multi-characterization approach is attractive because measurements are taken simultaneously on each single sample, thereby reducing the uncertainty that could arise from needing different samples or experimental setup for measuring different properties. The dataset generated from this study would help compare trends between synthetic and natural samples, although only restricted conclusions can be drawn based on the limited number of samples studied.

2. Materials and Methods

2.1. Rock samples

In this study, we used two natural and two synthetic sandstone core samples of ~2 cm height, 5 cm diameter and porosities within the range 20-25% (Table 1). Berea and Corvio sandstones were the selected materials to represent homogeneous, highly isotropic natural sandstones of well-known properties. While Berea has been historically used as standard in rock physics experiments (e.g., Christensen and Wang 1985), the latter has been recently recognized as a potential standard sandstone (Falcon-Suarez et al. 2017a).

The original goal of our synthetic sandstones was to obtain a cohesive granular pack of well-known properties to characterize the ultrasonic properties of rock samples with controlled fracture geometry (Tillotson et al. 2011, Tillotson et al. 2012). These data were used to challenge Chapman's (2003) theory based on squirt flow mechanisms in anisotropic porous rocks (Chapman 2003). A uniform granular distribution is preferred when comparing laboratory data and theory, particularly in Chapman's model where grain size is an intrinsic parameter. Thus, we used Leighton Buzzard sand with grain size varying between 90 – 150 μm, a highly uniform granular material small enough to ensure the wavelength (5 and 3 mm for P and S-wave, respectively) is much larger than the grain size, to satisfy effective medium theory.

The synthetic sandstones were manufactured at the National Oceanography Centre, Southampton (NOCS) using the methodology outlined by Tillotson et al. (2012). The fabrication process comprises the following three steps.

First, the Leighton Buzzard sand (Q), sodium silica gel (NaSi) and kaolinite (Ka) are mixed satisfying the total mass equals to X_Q+0.25X_Q(NaSi)+0.1X_Q(Ka), where X_Q represents the mass of sand and 0.25 X_Q and 0.1X_Q the relative mass factors for NaSi and Ka, respectively. The mixture is stirred in two steps: i) NaSi and Ka are

mixed using an electric mixer until a milky-looking mixture is obtained (well-spread clay in gel); ii) Q is then added and the three components mixed together during certain time for homogenization.

Second, the resulting mixture is poured into a stainless steel cylinder (5 cm diameter mould) and axially compressed to 5 MPa, under constant oedometric conditions until stabilization.

Finally, the mould with the compressed sample is heated in the oven up to 275 °C - increasingly from lab temperature at a constant rate 10 C d^{-1}, to transform NaSi and Ka into solid silica cement. After cooling down (3 to 4 days) and demoulding, the resulting plug is DIW-flushed to remove non-cemented particles and impurities.

This technique has the advantage that the sample is cemented under a preselected load that could be representative of certain diagenetic conditions. Also, our technique uses a benign low temperature for cementation (275° C), compared to previous methods in which heating above the melting point of glass (950° C) was required for synthetic sandstones (den Brok et al. 1997). After the manufacturing process, the sample is finally exposed to atmospheric conditions with negligible stress release-induced damage, as they are strongly bonded. This particular bonding effect may be because there is generally more cement present in these synthetic sandstones than in nature for an equivalent porosity, resulting in over-stiffness (Falcon-Suarez et al. 2017b).

The four samples were subjected to flooding tests under variable conditions of confining and pore pressure as detailed below. Before and after, different techniques were used to complete the characterization of the samples, including: (i) porosity by He-pycnometry, mineralogy (X-ray diffraction analysis with a Philips X'Pert pro XRD - Cu X-ray tube), thin sections and 3D X-ray micro-CT imaging (micro-focus Custom

Nikon HMX ST Scanner), determined in the facilities at the NOCS; and (ii) pore size distribution by Hg-porosimetry (Micromeretics Hg-injection porosimeter) and permeability (vertical, k_v, and horizontal, k_h) to nitrogen under minimal confining (~0.7 MPa), measured in the Wolfson Multiphase Flow Laboratory, University of Leeds. The basic physical properties and composition of the four samples are shown in Table 1. The theoretical dry density of the solid particles (ρ_s) was estimated from the average percentage of each mineral phase (XRD) as $\rho_s = \rho_d/(1-\phi)$), using mineral densities repeated in the literature.

Table 1. Physical properties of the synthetic (Syn-1 and Syn-2) and natural (Corvio and Berea) sandstones.

Sample	ρ_s	ϕ	$^*k_v$ / k_h	Mineral-XRD (%)			
	(kg m^{-3})	(%)	(mD)	Quartz	Albite	Muscovite	Kaolinite
Syn-1	2651	0.255	0.8 / 15	87.6	0.4	3.5	8.5
Syn-2	2651	0.226	1.6 / 11	87.7	0.5	3.4	8.4
Corvio	2649	0.215	260 / 325	97.6	-	-	2.4
Berea	2653	0.198	275 / 300	91.2	0.2	3.6	5.0

* k_v and k_h, vertical and horizontal permeability

The four samples used in this study were equipped with one set of 90° bi-axial 350 ohm electrical strain gauges each, epoxy-glued on the lateral side of the sample to measure axial and radial strains during the flooding test.

2.2. Experimental setup

The test was performed using the experimental setup shown in Figure 1. The rig is assembled around a triaxial cell core holder that allows housing 5 cm diameter rock samples up to 65 MPa of confining and pore pressure. Inside the vessel, a 6 mm wall, 190 mm height NHBR rubber sleeve isolates the core plug from the confining fluid (mineral oil). The sleeve is perforated with 16 stainless steel

electrodes which, once in contact with the sample, provide electrical resistivity tomography measurements (North et al. 2013). Under typical operating conditions the resistivity measurement error is ~5 % for samples in the electrical resistivity range 1-100 Ω m.

The sample is axially confined with two platens housing the ultrasonic pulse-echo sensors. The core plug is isolated from the rest of the rig and the ultrasonic transducer by two PEEK buffer rods. These buffer rods have well defined acoustic impedance and low energy loss, providing a reliable delay path to enable the identification of top/base sample reflections for calculating ultrasonic P- and S-wave velocities and attenuations using the pulse-echo technique (Best 1992). The technique provides useable frequencies between 300 - 1000 kHz. Within this range, the velocity precision is ±0.1% and the accuracy is ±0.3% (95% confidence), while the attenuation accuracy is ±0.1 dB cm^{-1} (Best 1992). Under saturated conditions, both the velocity and attenuation are frequency dependent properties (Chapman 2003). Within the high frequency range considered here, “squirt flow mechanisms” may lead to dispersion in the experimental data (Best 1992, Falcon-Suarez et al. 2016), particularly in the presence of fractures/cracks (Tillotson et al. 2011, Tillotson et al. 2014). These effects have to be taking into consideration when upscaling results to the (seismic) low-frequency band (Guéguen and Schubnel 2003). In this study, we compare the ultrasonic properties of the four samples using the pulse-echo technique at a single frequency of 600 kHz, obtained from Fourier analysis of broad band signals.

The axial platens are configured to bypass the leads from the strain gauges on the side-wall of the rock samples. The leads are connected to a 4-channel data

acquisition system (Vishay-Model D4). Besides, the platens and buffer rods implement fluid pathways that allow pore fluid circulation across the sample.

Both the confining and pore pressure are controlled by dual ISCO EX-100D systems; and an extra ISCO ED100 cylinder is used as backpressure downstream of the sample. Axial and radial confining stress (σ_1 and $\sigma_2=\sigma_3$, respectively) can be independently applied to the triaxial vessel, although for this experiment we used a hydrostatic configuration ($\sigma_1=\sigma_3=\sigma_c$). Pore fluid is delivered/received using fluid transfer vessels (FTVs) to minimize fluid-induced corrosiveness effects on the equipment. For this experiment, a FTV is used for delivering, flushing the rock samples with 35 g L^{-1} NaCl solution (synthetic brine) upstream, while another FTV is used for receiving downstream.

To further control the pore pressure, two piezo-resistive pressure transmitters (Keller model PA-33X) are located in the pipeline up and downstream of the sample, very close to in- and outlet ports. Thus, combining the pressure gradient (ΔP), the volumetric flow rate (Q) and the properties of the sample and pore fluid, permeability (k) can be calculated using the well-known steady state flow method based on Darcy's law:

$$k = \frac{\mu L Q}{\Delta P A}, \qquad (1)$$

where μ is the dynamic viscosity of the fluid, and L and A, the sample length and area, respectively.

2.3. Test configuration

Ultrasonic P- and S-wave velocities (V_p and V_s) and attenuations (inverse quality factors Q_p^{-1} and Q_s^{-1}), electrical resistivity, axial (ε_a) and radial (ε_r) strains,

and permeability (k) were measured for a defined stress path on the four samples (brine saturated), covering confining stress (σ_c) and pore pressures (P_p) within the range 15-50 MPa and 5-10 MPa, respectively. To configure the stress path of the experiment, we conducted an exploratory test under dry conditions through a hydrostatic loading test within the range 5-50 MPa, using V_p and V_s to analyse the stress-dependency of the four samples (Figure 2). We distinguished different trends between natural and synthetic samples. While the synthetics show quasi- linear trends, the naturals exhibit an initial abrupt increase of the velocities, likely associated with microcracks closure mechanisms occurring at early loading stages (Falcon-Suarez et al. 2017a, Prasad and Manghnani 1997). Quasi-linear behaviours during loading have been related to elastic stiffening of the individual minerals of the rock beyond the microcracks closure stress limit (Vernik and Hamman 2009); however, in the case of the synthetic sandstones, it might be attributed to the absence of microcracks due to the gentler stress-release process (no coring) applied during the manufacturing process. The assessment of the data from this exploratory test will be further addressed below through effective medium theories (EMT) and the grain-to-grain contact modelling.

Focusing on the natural sandstones, we arbitrarily selected four *quasi*-linear sections (zones I to IV, Figure 2) to configure a stress path with four sub-paths (sequences). Each stress sequence is designed to satisfy changes in the differential pressure ($P_{diff} = \sigma_c - P_p$) keeping constant the pore pressure and *vice versa* (see Figure 3), also accounting for positive (loading) and negative (unloading) gradients. Thus, the effective stress coefficient can also be used to analyse the interplay of confining and pore pressure on the samples, according to the following expression (Todd and Simmons 1972):

$$n_{(\beta)} = 1 - \frac{\partial\beta / \partial P_p \Big|_{P_{diff}}}{\partial\beta / \partial P_{diff} \Big|_{P_p}}, \quad (2)$$

where β is any measured property of the sample.

After the exploratory test, the samples were saturated with degassed 35 g L^{-1} NaCl brine via water imbibition in a vacuum vessel. Then, k, ε_a and ε_r were monitored continuously, whereas V_p, V_s, Q_p^{-1}, Q_s^{-1} and (immediately after the ultrasonic properties) resistivity were systematically measured at the end of each stress state. Volumetric deformation (ε_v) was also calculated as $\varepsilon_v = \varepsilon_a + 2\varepsilon_r$, which can be considered as equivalent to the mechanical variation of porosity (ϕ) under such chemically non-reactive conditions.

Variations of the stress state were carefully controlled by the (ISCO) pumping systems. This aspect is crucial because the rate of stress changes are expected to affect the confining and pore pressure dependency of any measured variable (Todd and Simmons 1972). Thus, the more rapid the pressure equilibrates the more stable the results yielded, which is particularly significant in poorly connected pores/cracks media. For these experiments, we applied a gentle loading/unloading stress and pore pressure rates of ~0.05 MPa s^{-1}, under drained conditions. Also, after every change in the stress state, we waited 30 min before starting the ultrasonic and resistivity measurements. This period was considered time enough for our samples to equilibrate after observing steady values of strains, and also the permeability through the stabilization of the pore pressure at constant flow (0.5 cm^3 min^{-1}). All in all, the effective time for a whole test was ~10 hours.

2.4. Data analysis

Multiple linear regressions were carried out on each of the sample properties (V_p, V_s, Q_p^{-1}, Q_s^{-1}, resistivity, k, ε_a, ε_r and ε_v) to further analyse the trends of the different samples and types of sample (natural versus synthetic) with respect to changes in σ_c and P_p. But, as observed during the exploratory test, stress dependency of wave velocities requires a non-linear stress-strain relationship. Such trends are driven by porosity changes, grain rearrangement and loading induced-cracking, in dry rocks (Holt et al. 2005); saturated samples are also influenced by the fluid composition and pore pressure, which characterize the bulk modulus of the sample (Xu et al. 2006).

Quadratic terms were introduced to account for these non-linear relationships. Non-significant variables were excluded from the model through stepwise backward selection (Crawley 2007). All analysis were conducted in the statistical software R (Team 2016), using a similar approach to Falcon-Suarez et al. (2017b).

3. Experimental results

Figure 3 shows the results obtained in the four tests. In absolute values, we observe very little differences between natural and synthetic sandstones in terms of ultrasonic properties and strains, but large differences in resistivity and, particularly, permeability.

In all cases, the samples properties behave with the increasing stress as expected. V_p and V_s increase with the differential pressure, while Q_p^{-1} and Q_s^{-1} show the contrary. Corvio sandstone shows the highest variations in V_p and V_s, increasing by ~11% and ~17% at the maximum P_{diff}, respectively; for the rest of the samples, this range remained below 9%. Corvio also shows the highest change in Q_s^{-1}, by ~62% at the maximum P_{diff} (i.e., ~8% more than the other samples). Q_p^{-1} varied

within the range 54-65% depending on the sample, with highest values Syn-1 and Berea. Likewise, the velocities show more significant variations for P_{diff} <30 MPa in all cases, but particularly for natural sandstones. Similarly, the attenuations decrease (approximately) linearly for the synthetics, while a sharp drop on the naturals at early loading stages (constant brine saturation conditions) reveals more significant microcrack closing mechanisms in these samples.

Resistivity and k evolve inversely with stress. The trends suggest a typical stress-induced pore connectivity reduction with increasing loading, which leads to permeability reduction down to 86% at the maximum P_{diff} for Syn-1, and resistivity increases of ~30% for Syn-1 and Syn-2. With the exception of Syn-2, all the studied samples show a sharp drop in permeability, coinciding with a deviation between ε_a and ε_r. At these turning points, axial deformation becomes more significant for Syn-1, Corvio and Berea, resulting in partial collapse of the main flow pathways; while Syn-2 shows *quasi*-isotropic deformation (i.e., $\varepsilon_a = \varepsilon_r$) and its permeability reduction occurs progressively up to ~25% at the maximum P_{diff}, but smaller than the other samples (above 50%).

3.1. Microstructural analysis

Figure 4a shows that all samples exhibit large amount of Hg-injected volume at low entry pressure corresponding to 10 microns (μm) pore size; however, pore size distribution offers a different perspective, whereby most of the pore throats are very much smaller (<0.1 μm) and are likely to have a more significant effect on the stress-related permeability and resistivity behaviours. In this regard, we observe a similar PSD range for Syn-2 and Corvio (0.5 - 0.01 μm), and for Syn-1 and Berea (<0.01 μm), which could suggest similar transport properties for the two formers and

likewise for the latter samples. However, the permeability to gas under non-stress conditions indicates a clear difference between synthetic and natural samples, with lower absolute values and higher permeability anisotropy for the synthetics. However, the permeability to gas under non-stress conditions indicates a clear difference between synthetic and natural samples, with lower absolute values and higher permeability anisotropy for the synthetics (Table 1). This discrepancy suggests the pore connectivity is poorer in the synthetics, particularly in the vertical direction.

The cumulative porosity distribution of Corvio sample agrees with the data presented by Falcon-Suarez et al. (2017a), while Berea sample shows a similar cumulative distribution to that reported in previous works (e.g., Madonna et al. 2012, Delle Piane and Sarout 2016). Synthetic sandstones have discontinuous grain size distributions, with the absence of populations between 2 and 7 μm (see dark band in Figure 4a). In both cases, we observe a sharp increase between 0.1 and 0.5 μm, more prominent for Syn-2, which could be indicative of a dual porosity effect for the synthetics (at ~10 μm and ~0.2 μm, respectively). This interpretation is supported by CT-scan images (Figure 4b), where we distinguish two pore size families in the case of the synthetics (see 1 and 2 for lower and higher sizes, respectively, in Figure 4b), and a more uniform pore size distribution across the range for the natural sandstones.

Further insights of sample textures are obtained from thin section observations (Figure 5). Berea has coarser grain size than Corvio, both with sub-angular grains, while the synthetics are more well-sorted sandstones with a finer grain size (~100 μm). The natural sandstones appear to have a wider span of grain sizes compared to the synthetics. The presence of phyllosilicates is only visible in

Berea (central areas of Figure 5 g-h), since in the synthetics the clay portion is forming the cement. The grains of the synthetic sandstones are visually coated by the cement, covering more contact area in Syn-2. The presence of inter-granular cement in the natural samples is more evident in Corvio.

The synthetic samples show a larger pore size range with local compaction bands, approximately perpendicular to the flow direction (blue arrow in Figure 5). Induced compaction bands have been found to occur in sandstones between 20-28% porosity during triaxial conditions (Fortin et al. 2007). As we used hydrostatic conditions for our experiments, the compaction bands can be explained as a manufacturing-induced effect, as a result of the oedometric pressurization conditions applied during sample preparation. Grain-to-grain contacts forming arches (Terzaghi et al. 1996) are visible on top of these sub-horizontal apertures. That prevents the open-space from collapsing during loading. The formation of stress-induced arch-like structures is also linked to the axially-forced grain-driving during sample preparation instead of natural gravitational deposition. Another difference between synthetic and natural samples is the intra-granular cracks. Only Corvio and Berea samples show some degree of damage (microcracks), more significant in the latter case, but still an expected feature of rocks formed under natural geological conditions.

Bolton et al. (2000) found that over-consolidated fine-grained sediments without a compactional fabric but favourably aligned microfractures (enhancing the flow when aligned in this direction) can show anisotropy permeability by a factor of 10. Reciprocally, the absence of aligned microcracks in our synthetic sandstones suggests the rock fabric might be affecting the transport properties. The smaller grain size and higher angularity have been reported as the main features of our synthetics samples to support their lower permeability and high porosity with respect

to natural analogues (Amalokwu et al. 2016, Amalokwu et al. 2014, Tillotson et al. 2014, Falcon-Suarez et al. 2017b, Falcon-Suarez et al. 2016, Tillotson et al. 2012). However, thin-section analyses illustrates that cement distribution and the presence of sub-horizontal compaction-induced bands are also significantly affecting the flow properties in the vertical direction (i.e., in this case, the direction of compaction during the manufacturing), resulting in anisotropic permeability (see Table 1).

3.2. Statistical analysis

Confining stress (σ_c), differential (P_{diff}) and pore pressure (P_p) had significant effects on all sample properties (V_p, V_s, Q_p^{-1}, Q_s^{-1}, ε_a and ε_v), although only the relations between variables with P_c are shown in Figure 6, with P-values <0.001 in all cases (see Table 2). V_p, V_s, Q_p^{-1}, Q_s^{-1}, ε_a and ε_v show variable degrees of non-linear relationships with P_c, with differences between samples observed for all properties. Permeability was the only property unaffected by P_p in all samples.

In general, differences between natural and synthetic samples in response to σ_c and P_{diff} seem to exist for resistivity and permeability, although differences between samples remain largest.

Table 2. R^2 obtained for each based on multiple regression analysis

	V_p	V_s	Q_p^{-1}	Q_s^{-1}	Resistivity	k	ε_a	ε_r	ε_v
* P_{diff}	0.994	0.988	0.980	0.965	0.995	0.988	0.974	0.959	0.984
* σ_c	0.994	0.989	0.982	0.964	0.993	0.990	0.988	0.968	0.988

* Note: P-value <0.001 in all cases.

3.3. Effective stress coefficient

Table 3 shows the effective stress coefficient (n) for ultrasonic P- and S-wave velocities (V_p, V_s) and attenuations (Q_p^{-1}, Q_s^{-1}), electrical resistivity, permeability (k)

and axial (ε_a) and radial (ε_r) strains and porosity (ϕ), for the four sandstones. The values represent the average of the four n-values per stress sequence derived from the P_{diff} and P_p gradients (see Figure 2).

Table 3. Effective stress coefficients for the measured parameters

P_{diff} (MPa)	V_p	Q_p^{-1}	V_s	Q_s^{-1}	Resistivity	k	ε_a	ε_r	ϕ
Syn-1									
10 - 15	0.9 ±0.1	0.7 ±0.1	1.3 ±0.6	1.1 ±0.5	0.9 ±0.1	2.0 ±3.0	1.2 ±0.3	0.6 ±0.1	0.7 ±0.1
20 - 25	1.0 ±0.0	0.7 ±0.1	1.1 ±0.1	-3.4 ±8.0	0.9 ±0.8	1.0 ±0.0	2.7 ±0.4	0.6 ±0.2	0.9 ±0.2
30 - 35	0.5 ±0.4	0.4 ±0.6	0.6 ±0.4	1.0 ±0.4	0.6 ±0.7	1.1 ±0.6	7.3 ±3.0	0.5 ±0.2	0.7 ±0.3
45 - 45	0.9 ±0.1	-1.4 ±0.6	1.1 ±0.2	2.0 ±2.0	1.5 ±0.2	1.2 ±0.6	2.2 ±0.4	0.6 ±0.2	1.0 ±0.3
Syn-2									
10 - 15	0.9 ±0.1	1.6 ±0.2	0.8 ±0.1	0.8 ±0.3	2.1 ±3.0	1.0 ±1.0	0.9 ±0.0	2.1 ±1.4	1.3 ±0.5
20 - 25	0.9 ±0.1	1.8 ±0.6	1.1 ±0.1	1.8 ±0.5	1.5 ±1.4	0.9 ±0.3	0.9 ±0.1	6.2 ±0.8	2.3 ±0.1
30 - 35	0.9 ±0.1	0.4 ±0.3	1.0 ±0.1	4.6 ±2.0	2.0 ±0.5	3.8 ±2.3	1.1 ±0.0	21 ±2.0	2.9 ±0.2
45 - 45	1.4 ±0.9	2.1 ±0.4	1.0 ±0.3	0.1 ±1.0	1.9 ±0.1	0.3 ±1.0	0.6 ±0.5	-7.3 ±9.0	2.4 ±0.8
Corvio									
10 - 15	1.0 ±0.1	1.0 ±0.0	0.9 ±0.1	1.0 ±0.2	0.6 ±2.3	-2.4 ±8.0	0.1 ±0.3	0.7 ±0.6	0.3 ±0.4
20 - 25	1.1 ±0.0	1.1 ±0.0	1.0 ±0.0	1.0 ±0.1	2.2 ±0.2	-2.5 ±7.0	0.1 ±0.1	3.9 ±1.6	1.2 ±0.1
30 - 35	1.1 ±0.1	2.3 ±0.5	1.0 ±0.0	1.1 ±0.0	-0.2 ±3.9	0.4 ±0.7	0.3 ±0.2	-2 ±0.3	1.8 ±0.5
45 - 45	1.0 ±0.0	0.9 ±0.0	1.0 ±0.0	1.3 ±2.0	1.0 ±0.3	0.8 ±2.0	0.1 ±0.0	-1.8 ±1	1.0 ±0.6
Berea									
10 - 15	0.5 ±0.5	0.5 ±0.4	0.4 ±0.4	0.4 ±0.3	2.8 ±3.5	-6.5 ±5.0	0.6 ±0.1	1.6 ±0.1	1.1 ±0.0
20 - 25	1.0 ±0.0	1.3 ±0.1	0.9 ±0.0	0.8 ±0.2	1.9 ±1.0	1.0 ±0.8	0.6 ±0.0	2.8 ±0.4	1.3 ±0.1
30 - 35	0.8 ±0.1	0.7 ±3.0	0.9 ±0.0	0.9 ±0.2	0.9 ±1.2	-2.5 ±0.5	0.6 ±0.2	0.6 ±0.0	0.6 ±0.0
45 - 45	0.6 ±0.1	0.9 ±0.4	0.8 ±0.0	0.3 ±0.4	-1.3 ±6.1	-0.3 ±0.4	0.5 ±0.2	0.5 ±0.0	0.5 ±0.1

Wave velocities have *n* values below unity, which agrees with previous experimental data on sandstones (Christensen and Wang 1985, Prasad and Manghnani 1997). Attenuations show more dispersion around one, which is less consistent with the scarce experimental work reported in the literature (Prasad and Manghnani 1997). Such dispersion also extends to resistivity and permeability, with values preferentially above unity. This observation agrees with the theoretical

approach of Berryman (1992), and the experimental data and modelling presented by Al-Wardy and Zimmerman (2004) for permeability in up to 10% clay-rich sandstones. Axial strains remain mostly below unity, in agreement with previous observations (e.g., Ma and Zoback 2017), showing very little variations with P_{diff} in all cases but Syn-1. Radial strains vary significantly with the increasing stress for all samples except Syn-1; the dispersion derived by radial strains is translated into porosity as we can consider it a proxy of volumetric strain (at the relative small stress levels used in our experiments).

As expected, n values vary from one property to another (Ma and Zoback 2017). Theoretically, we can make a simple division of the analysed properties into two groups (Glubokovskikh and Gurevich 2015): scale-dependent (permeability and resistivity), and scale-independent (ultrasonic waves and strains) properties. We expect for a porous medium that is homogeneous, isotropic, with a linearly elastic frame, that under drainage conditions, the effective stress coefficient n = 1 only for the scale-independents (Berryman 1992, Glubokovskikh and Gurevich 2015). Glubokovskikh and Gurevich (2015) suggest that the meaning beyond n < 1 for the scale-independent properties is the violation of any of the previous assumptions.

Assuming no physico-chemical alterations due to rock-fluid interaction, we should expect clear differences of the effective stress coefficient between synthetics and natural sandstones, based on the microstructure, but we should see similarities between individual groups. However, we observe no similarities between both groups, for any of the properties. Our results have been obtained from the variations of the measured parameter between two pore pressures per stress sequence (see Figure 2), which implies our estimations of the effective stress coefficient are very sensitive to the quality of the measurements. The accuracy of the elastic wave

determination is higher than that for the rest of the parameters. Resistivity and permeability measurements carry associated larger errors, which is reflected in some values either very high or below zero. The strain gauges have a precision of ~0.1%, but we observe high dispersion in the radial deformation in Syn-2 and Corvio and in the axial in Syn-1. Among all the possible explanations for the anomalies in the strains, we emphasize the potential over-stiffness effect associated with the low length-to-diameter ratio (~0.4) of our samples (Falcon-Suarez et al. 2017b).

4. Micromechanic elastic assessment

The mechanical response of bulk sandstones is not linear even for the elastic regime because under hydrostatic loading rock compressibility decreases with stress (Wong et al. 2004). Such behaviour depends on multiple intrinsic properties of the porous media, including cement content, porosity, grain size, cracks and pore fluid. Although microcracks typically represent less than 1% of the total porosity of many sandstones, they are particularly compliant, which might have significant effect on their elastic properties (Fortin et al. 2007). The silica cement on synthetic sandstones has been found to enhance rock strength, even shifting the brittle-to-ductile transition towards higher pressures (David et al. 1998). However, it is not only the amount of cement that affects the mechanical properties of sandstones; its distribution within the granular matrix as well as the grain-to-grain contact features also has a crucial effect (den Brok et al. 1997, David et al. 1998).

In this section, we address the elastic behaviour of our samples during the exploratory test (dry conditions), to identify additional criteria to explain discrepancies between synthetic and natural sandstones. We use two complementary (modelling) approaches to investigate (i) the effect of microcracks compliance based on effective

medium theories (EMT), where the sample is treated as a continuous matrix with pores and cracks; and (ii) the bounding at the interparticle contact, where the sample is considered as a discontinuous granular medium (Fortin et al. 2007).

4.1. Effective moduli of dry samples: "cracks and pores" model

EMT models allow the relation between elastic properties of rocks and their intrinsic microstructural features such as porosity, microcracks or pore fluid (Fortin et al. 2007, Guéguen and Schubnel 2003). These properties are stress dependent parameters and therefore through EMT, we can understand the behaviour of rocks under variable stress conditions. We applied the EMT "cracks and pores" model used by Fortin et al. (2007) to study the crack density effect during compression under dry conditions.

The "cracks and pores" model is based on the effective matrix non-interacting model and assumes solid grains, spherical pores and penny-shaped cracks, where the elastic potential results from the sum of the individual pore and crack potentials (Kachanov 1993). The model has a broad range of validity and field of application because at random distributions and high crack densities, the individual effect of local tensile stress is globally cancelled (Guéguen and Schubnel 2003). Further aspects of the theory can be found in Fortin et al. (2007) and references therein.

The representative elementary volume (REV) symbolizes the minimum sample volume containing enough microstructural attributes (microcracks, pores and grains in our case) that allows the effective properties calculation to be applied (Wong et al. 2004). The crack density expresses the volume of cracks (V) per REV in a sample such as $\rho=V^{-1}\Sigma^{n}(c_i^3)$, where c_i is the radius of every singular (i) crack and n the total number within the REV (Fortin et al. 2007).

Using V_p and V_s from our dry test and estimated sample bulk densities, the elastic moduli of the bulk material can be easily calculated (e.g., Falcon-Suarez et al. 2017b). Then, the micromechanical and elastic parameters of the sample can be related using the following expressions (Fortin et al. 2007):

$$\frac{K}{K_m} = 1 + \frac{\rho}{1-\phi}\frac{h}{1-2\nu_m}\left(1-\frac{\nu_m}{2}\right) + \frac{\phi}{1-\phi}\frac{3\left(1-\nu_m\right)}{2\left(1-2\nu_m\right)}, \quad (3)$$

$$\frac{G}{G_m} = 1 + \frac{\rho}{1-\phi}\frac{h}{1+\nu_m}\left(1-\frac{\nu_m}{5}\right) + \frac{\phi}{1-\phi}\frac{15\left(1-\nu_m\right)}{7-5\nu_m}, \quad (4)$$

where ν, K and G are the Poisson's ratio, and bulk and shear moduli of the material. The subscript *m* refers to the elastic constants for the crack and porosity free matrix, and *h* is the factor describing the penny-shaped geometry as:

$$h = \frac{16\left(1-\nu_m^2\right)}{2\left(1-\nu_m/2\right)}. \quad (5)$$

For sandstones within the porosity range 20-25%, microcracks would represent only 0.2 to 0.3% of the total porosity (Wong et al. 2004), so that crack volume variation is negligible compared to pore volume. Additionally, the bigger microcracks compliance commonly occurs at early stages of hydrostatic loading. Hence, assuming the highest velocities obtained during hydrostatic loading (at 50 MPa) are representative of a continuous crack-free matrix of known porosity, we can calculate K and G to estimate K_m and G_m (Table 4).

Table 4. Computed elastic constants for the crack-free matrix

Sample	K_m (GPa)	G_m (GPa)
Syn-1	18.8	18.8
Syn-2	17.1	18.7
Corvio	17.1	18.9

Berea	20.9	20.6

Figure 7a shows the “cracks and pores” model prediction at the corresponding porosity of each sample (Table 1) together with the projection of the experimental data. The model predicts that the crack density of natural samples is higher than the synthetics for either bulk modulus (K/K_m) or shear modulus (G/G_m), varying as Syn-1 < Syn-2 < Corvio < Berea. Figure 7b shows that, at the lowest confining stress (σ_c = 5 MPa), the natural sandstones have a crack density $\rho > 0.4$. Between 5 and 15 MPa, this value drops by ~60% for Corvio and up to 75% for Berea. The crack density of the synthetics sandstones varies more linearly. Above 15 MPa, the crack populations of the four samples behave similarly with increasing confining stress. Slight differences between Syn-2 and Corvio, and Syn-1 and Berea are also distinguished by the effective bulk modulus (K/K_m) adjustment.

4.2. Grain-to-grain contacts

The Digby’s contact model (Digby 1981) assumes a random packing of identical elastic spheres of radius *R* originally bonded (cementation) by ideal discs of radius *b*. Upon hydrostatic compression the packing increases and the initial contact area increases from radius *b* to *a*, meeting the criteria $b < a < R$. Then, the model relates ultrasonic velocities and the packing through the following expression:

$$\left(\frac{V_p}{V_s}\right)^2 = \frac{3\frac{a}{b}\left(2-\nu_g\right)+4\left(1-\nu_g\right)}{\frac{a}{b}\left(2-\nu_g\right)+3\left(1-\nu_g\right)}, \qquad (6)$$

where ν_g is the Poisson’s ratio of the grains.

In Figure 8, we present the evolution of the V_p/V_s ratio with the confining stress together with its variation with ν_0 for different a/b values. Also, we plot the V_p/V_s -

stress curves inferred from the “cracks and pores” model (Figure 7a,b). V_p/V_s evolution gives complementary information about rock compaction. We observe an increasing V_p/V_s ratio with stress as a consequence of the viscoelastic closure of the original microcracks (Fortin et al. 2007) in the four samples. Syn-1 and Berea reaches an asymptotic value ~15 MPa, while for Syn-2 and Corvio the V_p/V_s ratios continue increasing. These trends would indicate a more gradual crack closure in the latter case, which disagree with our previous estimates regarding crack density distributions (Figure 7). Alternatively, it could be also related to the performance of a more randomly oriented crack population for Syn-2 and Corvio, or different pore shapes. From the cementation and grain contact approach, we also observe evidences of lower degree of compaction for Syn-2 and Corvio. In all samples, the a/b ratio increases between 0.4 and 0.6 (Figure 8). But, Syn-2 shows the highest variation (~50%), followed by Corvio (~35%) and then Syn-1 and Berea both with similar levels (~20%).

On the whole, the grain-to-grain contact analysis shows no clear separation between the behaviour of the synthetic and natural sandstones. Our EMT model predicts better Syn-2 and Corvio than Syn-1 and Berea. However, in all cases, the EMT model prediction is better at high pressure whereas underestimates the experimental data during the early loading stages (Figure 8). Similar discrepancies at low stress conditions are also reported by Fortin et al. (2007).

5. Discussion

The similar responses of the elastic properties to stress variation of the studied synthetic and natural sandstones suggest that the synthetic sandstones may be good alternatives to their natural analogues, for certain laboratory tests. However,

this is not the case when considering transport properties. The lower permeability and higher resistivity of the synthetics reveal a less developed pore connectivity and higher heterogeneity their natural analogues.

As pointed out by Amalokwu (2016), the relatively high porosity low permeability of the synthetic samples may be counter-intuitive but it is consistent with observations in natural rocks and sediments. Porosity generally tends to increase with decreasing grain size for sands of uniform grain size. By contrast, permeability decreases with decreasing grain size as pore throats are smaller in finer sediments, with the higher capillary attraction of the walls inhibiting flow (Chilingarian and Wolf 1976). Our synthetic rocks contain small and uniformly-sized grains compared to the natural rocks (Figure 4b).

Crawford et al. (2008) found the permeability reduction observed upon loading from 5 to 50 MPa was strongly dependent on the clay content. Although our synthetic samples have 3 to 5% more clay than the natural ones, this small difference is insufficient to explain a two orders of magnitude difference in the permeability (see Dautriat et al. 2009). Further, while even such small increment of clay content would lead to decrease the electrical resistivity (Börner et al. 2013), we observe the opposite. However, the clay is used to form the cement of our synthetic sandstones and it is therefore incorporated into the rock skeleton. Thus, the clay excess is rather indicating that these samples are over cemented, which suggests that reducing the amount of kaolinite in the mixture could lead to a more representative material of the natural (transport and elastic) properties.

Compaction at early and intermediate stages of sedimentary burial is a (geologically) quick process which conditions flow properties of the resulting rock (Brzesowsky et al. 2014). Similarly, the precursor of our synthetic sandstones is a

non-consolidated sand subjected to fast compaction. In this case, the celerity of the process is much higher and clearly affects the rearrangement of grains. Grain rotation, sliding and shearing occur in both cases. But, natural burial allows for secondary processes such as creep, pore pressure modification, fluid substitution, or stress changes, all of which certainly influence the resulting granular packing. The stress-induced arch-like structures observed in the synthetic sandstones are the result of axially-driven forces (shear-enhanced compaction), which also affect the formation of compacting bands perpendicular to the axial direction. Consequently, the pore size distribution shows a dual porosity fabric. The lower pore size within the compacted bands is buffering the fluid connectivity through the sample. This observation is further supported by the anisotropic component of the permeability for synthetic samples reported in Table 1.

5.1. Elastic properties

In previous works, our synthetic sandstones have shown over-stiff behaviour attributed to the mineral framework and the manufacturing process (Falcon-Suarez et al. 2017b). However, this seems to be a minor effect according to the similar deformation patterns and absolute strain values shown by the four samples of this study. The porosity of the four samples reduces by 0.2-0.3% at the maximum differential pressure (Figure 3), a range that agrees with the porosity fraction associated with microcracks for sandstones with 20 to 25% porosity (Wong et al. 2004). This interval also agrees with the crack density reduction estimated from the “cracks and pores” model (Figure 7) of Fortin et al. (2007).

However, the variation of the crack density while increasing load has a different impact on the pores connectivity depending on the sample type (i.e., synthetics and

natural sandstones). The porosity to resistivity ratio (ϕ/Ω) at the maximum differential pressure is ~0.04% for the synthetics sandstone samples, but five times larger (~0.2%) for the naturals. This discrepancy let us conjecture that cracks have larger effect on the transport properties of our synthetic rocks. However, Wang et al. (2009) reported a ϕ/Ω ~2% for a ~24% porosity sandstone within the same range of pressures. Thus, even natural sandstones show a strong dependency between crack distribution and flow properties. In this regard, increasing the pore pressure for a constant confining of 20 MPa, we observe very little variations of permeability to pore pressure ratio (k/P_p) in the synthetics (<2%), and larger for the natural sandstones (>50%). For comparison, slightly higher k/Pp ratios were found by Al-Wardy and Zimmerman (2004) for Stainton sandstone (~90%), at the same conditions. We interpret these observations as the result of a more isolated cracks distribution in the synthetic sandstones than in the naturals, which leads to lower pore connectivity.

We can use the dynamic elastic constants of the rock to further investigate the deformation patterns of our samples. The elastic constants are more sensitive to the stress state and the stress path, composition, grain packing, type of pore fluid and crack density (Li and Fjær 2012). From the experimental data, we have calculated the dynamic Young's (E) and bulk (K) moduli (Figure 9), and normalized with the values presented in Table 5 to simplify comparisons. Since V_p/V_s ratio expresses the Poisson's ratio in isotropic media (Wang et al. 2012) and the shear modulus is equivalent to E, for simplification, we do not show these parameters.

E and K pressure dependent trends show no clear differences between the naturals and synthetic sandstones, although the synthetics behave similarly in both cases. V_p/V_s ratios remain approximately constant with the increasing stress for the synthetic sandstones, which contrasts with the decreasing trends of the natural

sandstones. The trends are reversed with respect to those observed under dry conditions (Figure 8), as expected. The asymmetry between dry and wet curves is more evident in the synthetic samples. This discrepancy might be related to the pore shapes of each type of rock, preferentially affecting V_p/V_s ratios under water saturated conditions (Wang et al. 2012). Despite that, the four samples tend towards similar V_p/V_s values with increasing load, which supports the idea that the absence/presence of micro-cracks is a major difference between synthetics and natural sandstones.

Q_s/Q_p ratios decrease with stress for the synthetics, while the opposite occurs with the naturals (Figure 9b). It can be interpreted as an increase in the P-wave quality factor (with stress) for the synthetic samples, and in the S-wave quality factor for the natural ones. Scattering attenuation becomes significant when the size of the heterogeneity becomes comparable to the elastic wavelength (Amalokwu 2016), which in our case would be mainly related to the crack aperture in the direction of the wave propagation. Based on the thin section images, the maximum crack aperture width we observe is ~0.25 mm, while in our ultrasonic pulse-echo experiments the wavelengths are approximately 5 mm and 3 mm for P-wave and S-wave, respectively. Then, the ratio of wavelength to crack aperture is ~25 and 16, respectively, suggesting the presence of microcracks should not significantly contribute to scattering attenuation (Amalokwu et al. 2016). However, while crack distribution is randomly oriented in our natural sandstones, some preferential crack elongation perpendicular to wave propagation is observed in the synthetics. In this regard, the stress-induced arch- bridge-like structures prevent the effective crack closure with stress in the axial direction. These features would be particularly affecting S-wave propagation perpendicular to the fractures (Amalokwu et al. 2014).

This effect can also be inferred from the crack density analysis under dry conditions. Initially, the shear modulus reflects larger crack density variations in our natural sandstones, while the bulk modulus does the same for the synthetics (Figure 7a-b). Upon loading, both tend to the same values for the four samples. Hence, crack closure improves S- to P-quality ratios (Q_s/Q_p) for the synthetics and the opposite for the naturals. Figure 9b also shows that Q_s/Q_p stabilizes above 15 MPa only for Syn-1 and Berea, which agrees with the V_p/V_s ratios under dry conditions (Figure 8). So, despite Q_s/Q_p being commonly used to determine the degree of saturation in rock samples (Amalokwu et al. 2014), it can also provide qualitative information about the interaction between ultrasonic waves and cracks in water saturated porous media.

In general terms, the elastic parameters of the synthetic sandstones are in good agreement with the natural ones used in this work, and with natural sandstones of similar porosities reported in the literature (e.g., Wang et al. 2009, Li and Fjær 2012, Falcon-Suarez et al. 2017a). The general trend is an increase in elastic moduli and ultrasonic velocities with increasing pressure, and the opposite for attenuations. The fact that the stress dependent ultrasonic properties are similar suggests that the dominant loss mechanisms are not significantly influenced by global fluid flow (Biot-type), but rather by local fluid flow loss mechanisms at this frequency (600 kHz), such as microcrack squirt flow. Nonetheless, in theory, the pressure dependence of synthetic rock velocities could be varied by altering the manufacturing process (Amalokwu 2016), including the generation of microcracks. On the other hand, Falcon-Suarez et al. (2017b) observed a softening of our synthetic sandstones under gentle loading/unloading cycles (within the elastic regime of the rock), only after the sample was exposed to brine. It is because the original (imposed) texture of the synthetic

sandstones leads to local anisotropic stress distribution during loading, with associated grain rearrangement through inter-granular sliding and grain rotation (Hangx et al. 2010, Brzesowsky et al. 2014), and the eventual generation of microcracks (including grain crashing) above a critical (hydrostatic) loading stress (Karner et al. 2003, Fortin et al. 2007).

Table 5. Initial values of the elastic parameters used in Figure 9.

Sample	$*E_0$ (GPa)	$*K_0$ (GPa)
Syn-1	21.8	12.9
Syn-2	23.8	14.1
Corvio	20.2	13.2
Berea	26.3	16.0

*Initial Young's and bulk moduli (E_0 and K_0, respectively), measured at P_c=20 MPa and P_p=10 MPa.

5.2. Anisotropy analysis

The manufacturing process of synthetic sandstones imposes compaction instead of free gravity-driven grain deposition of natural environments. Grain orientation is therefore forced when compressed into the manufacturing mould. Consequently, the synthetic samples encompass an anisotropic intrinsic feature. Our results suggest that this procedure affects less significantly the elastic and mechanical characteristics than the transport properties of the resulting rock.

Tillotson et al. (2012) and Amalokwu et al. (2016) have reported evidences of some degree of elastic anisotropy in our synthetic sandstones inferred from S-wave splitting analyses. To fully investigate the degree of anisotropy of the samples would require multidirectional core analysis (e.g., Wang 2002). However, our investigation was limited to a single core per rock sample examined in the vertical direction. A priori, compared to the natural sandstone samples, a greater degree of permeability anisotropy was observed for the synthetic samples when compared to the natural

samples (Table 1), although this statement is only valid for non-confining conditions. In any case, the uncertainty regarding the coring direction of the natural samples constrains our interpretation. Nevertheless, we are able to determine the full electrical resistivity tensor of our core samples using the method proposed by North et al. (2013).

The results of the anisotropy resistivity inversion data are presented in stereographic projection in Figure 10. We observe for all the samples a single high eigenvalue – highest resistivity defined by the dashed red line, interpreted as normal direction to the lamination. In all cases, the lamination plane includes the two symmetric low eigenvalues, indicating transversely isotropy resistivity for the four samples; weak for natural sandstones and high for synthetics, though. This fact supports the evidences of stress-induced lamination (layering) during synthetic sandstones manufacturing (compaction bands). However, it is not clear how this translates into elastic anisotropy, as the electrical anisotropy would mainly be representative of the transport properties.

5.3. Confining stress and pore pressure

The resistivity anisotropy analysis was performed at four differential pressures (P_{diff}) per sample. Each P_{diff} step was obtained several times per stress sequence, by modifying either the confining stress (σ_c) or pore pressure (P_p). Thus, in the anisotropy analysis, the individual effect of each change in condition is also considered (empty and solid symbols in Figure 10, for changes in P_p and P_c, respectively). In all cases, the effect of P_p on the anisotropy distribution is significant, and clearly distinguished from that derived from σ_c changes. This is in agreement with the effective stress coefficients above unity observed for resistivity.

The deformation behaviour of a rock differentially affects its elastic, mechanical and transport properties, which is expected to be reflected in the effective stress coefficient (Hofmann et al. 2005). Our attempt to use effective stress coefficients to investigate P_p and σ_c effects is limited by the narrow range of P_p available. However, our results still suggest that ultrasonic velocities and axial strain are preferentially constrained by changes in σ_c, and therefore effective stress coefficients are below unity. By contrast, permeability and resistivity are more sensitive to P_p changes: In the former case, the confining stress seems to progressively counteract the pore pressure effect with the increasing loading; in the latter, this effect is weaker but corroborated by the resistivity anisotropy tensor. Regardless the considered variable, for the conditions investigated in this work the effective stress coefficients show no specific differences between the synthetic and natural sandstones.

6. Summary and conclusions

We conducted a comprehensive laboratory multi-physics study of typical reservoir sandstones and two synthetic sandstones. A detailed comparison of the stress-dependence of geophysical, hydraulic and mechanical properties revealed important similarities and differences. The natural sandstones (Berea and Corvio) properties are influenced more by microcrack closure at low stresses, but otherwise show similar stress dependency for all measured parameters. However, there were differences in absolute permeability, resistivity and resistivity anisotropy for these similar porosity quartz sandstones, related to the synthetic sample manufacturing process. This fact makes these synthetic samples less suitable for hydraulic (fluid transport) property studies.

The resulting datasets have the potential to shed new light on cross-property relationships between ultrasonic (P and S-waves) velocities and attenuations, electrical resistivity, permeability, axial and radial strains, and derived properties, for a wide range of differential pressure.

Overall, the similarity in the elastic behaviour between the natural and synthetic sandstones increases the level of confidence when using synthetic rocks to assess reservoir rock properties. However, caution is required when studying transport properties using synthetic rocks. We observe significant differences in transport properties between natural and synthetic sandstones, which may be associated with stress-release induced-pathway (naturals) and a smaller and uniform grain size distribution with a slight layering parallel to the basal plane (synthetics). The layering is an effect associated with the manufacturing process, which also results in a higher degree of permeability and electrical anisotropy in the case of the synthetic samples. Effective stress coefficients, obtained for all the measured variables, are in agreement with theory and the limited experimental data available in literature. However, the narrow range of pore pressures used in this study is a limitation that needs to be addressed in future.

Acknowledgments

We have received funding from the UK's Natural Environment Research Council (grant NE/N016041/1 CHIMNEY and grant NE/R013535/1 GASRIP), the European Union's Horizon 2020 research and innovation programme (grant No. 654462 STEMM-CCS) and the project BIA2017-87066-R (MINECO/AEI/FEDER, UE). The authors thank Dr Yves Guéguen and an anonymous reviewer for their

constructive comments, and Philip Guise (Wolfson Multiphase Flow Laboratory, UL) for his valuable advice.

References

Al-Wardy, W. & Zimmerman, R.W. 2004. Effective stress law for the permeability of clay-rich sandstones. *Journal of Geophysical Research: Solid Earth* **109**, B04203.

Amalokwu, K., Best, A.I. & Chapman, M. 2016. Effects of aligned fractures on the response of velocity and attenuation ratios to water saturation variation: a laboratory study using synthetic sandstones. *Geophysical Prospecting* **64**, 942-957.

Amalokwu, K., Best, A.I., Sothcott, J., Chapman, M., Minshull, T. & Li, X.-Y. 2014. Water saturation effects on elastic wave attenuation in porous rocks with aligned fractures. *Geophysical Journal International* **197**, 943-947.

Amalokwu, K., Chapman, M., Best, A.I., Minshull, T.A. & Li, X.-Y. 2015a. Water saturation effects on P-wave anisotropy in synthetic sandstone with aligned fractures. *Geophysical Journal International* **202**, 1088-1095.

Amalokwu, K., Chapman, M., Best, A.I., Sothcott, J., Minshull, T.A. & Li, X.-Y. 2015b. Experimental observation of water saturation effects on shear wave splitting in synthetic rock with fractures aligned at oblique angles. *Geophysical Journal International* **200**, 17-24.

Amalokwu, K.J. 2016. *Saturation effects on frequency-dependent seismic anisotropy in fractured porous rocks.* Ph.D. thesis. University of Southampton.

Bernabé, Y., Fryer, D.T. & Hayes, J.A. 1992. The effect of cement on the strength of granular rocks. *Geophysical Research Letters* **19**, 1511-1514.

Berryman, J.G. 1992. Effective stress for transport properties of inhomogeneous porous rock. *Journal of Geophysical Research: Solid Earth* **97**, 17409-17424.

Best, A.I. 1992. *The prediction of the reservoir properties of sedimentary rocks from seismic measurements.* Ph.D. thesis. University of Reading.

Bolton, A.J., Maltman, A.J. & Fisher, Q. 2000. Anisotropic permeability and bimodal pore-size distributions of fine-grained marine sediments. *Marine and Petroleum Geology* **17**, 657-672.

Börner, J.H., Herdegen, V., Repke, J.-U. & Spitzer, K. 2013. The impact of CO_2 on the electrical properties of water bearing porous media – laboratory experiments with respect to carbon capture and storage. *Geophysical Prospecting* **61**, 446-460.

Brzesowsky, R.H., Spiers, C.J., Peach, C.J. & Hangx, S.J.T. 2014. Time-independent compaction behavior of quartz sands. *Journal of Geophysical Research: Solid Earth* **119**, 936-956.

Chapman, M. 2003. Frequency-dependent anisotropy due to meso-scale fractures in the presence of equant porosity. *Geophysical Prospecting* **51**, 369-379.

Chilingarian, G.V. & Wolf, K.H. 1976. *Compaction of coarse-grained sediments.*

Christensen, N.I. & Wang, H.F. 1985. The Influence of pore pressure and confining pressure on dynamic elastic properties of Berea sandstone. *Geophysics* **50**, 207-213.

Crawford, B.R., Faulkner, D.R. & Rutter, E.H. 2008. Strength, porosity, and permeability development during hydrostatic and shear loading of synthetic quartz-clay fault gouge. *Journal of Geophysical Research: Solid Earth* **113**, B03207.

Crawley, M.J. 2007. *The R book.* John Wiley & Sons Ltd.

Dautriat, J., Gland, N., Guelard, J., Dimanov, A. & Raphanel, J. 2009. Axial and Radial Permeability Evolutions of Compressed Sandstones: End Effects and Shear-band Induced Permeability Anisotropy. *Pure and Applied Geophysics* **166**, 1037-1061.

David, C., Menéndez, B. & Bernabé, Y. 1998. The mechanical behaviour of synthetic sandstone with varying brittle cement content. *International Journal of Rock Mechanics and Mining Sciences* **35**, 759-770.

Delle Piane, C. & Sarout, J. 2016. Effects of water and supercritical CO2 on the mechanical and elastic properties of Berea sandstone. *International Journal of Greenhouse Gas Control* **55**, 209-220.

den Brok, S.W.J., David, C. & Bernabé, Y. 1997. Preparation of synthetic sandstones with variable cementation for studying the physical properties of granular rocks. *Comptes Rendus de l'Académie des Sciences - Series IIA - Earth and Planetary Science* **325**, 487-492.

Digby, P.J. 1981. The Effective Elastic Moduli of Porous Granular Rocks. *Journal of Applied Mechanics* **48**, 803-808.

Falcon-Suarez, I., Canal-Vila, J., Delgado-Martin, J., North, L. & Best, A. 2017a. Characterisation and multifaceted anisotropy assessment of Corvio sandstone for geological CO_2 storage studies. *Geophysical Prospecting* **65**, 1293-1311.

Falcon-Suarez, I., Marín-Moreno, H., Browning, F., Lichtschlag, A., Robert, K., North, L.J. & Best, A.I. 2017b. Experimental assessment of pore fluid distribution and geomechanical changes in saline sandstone reservoirs during and after CO_2 injection. *International Journal of Greenhouse Gas Control* **63**, 356-369.

Falcon-Suarez, I., North, L., Amalokwu, K. & Best, A. 2016. Integrated geophysical and hydromechanical assessment for CO_2 storage: shallow low permeable reservoir sandstones. *Geophysical Prospecting* **64**, 828-847.

Fortin, J., Guéguen, Y. & Schubnel, A. 2007. Effects of pore collapse and grain crushing on ultrasonic velocities and Vp/Vs. *Journal of Geophysical Research* **112**, B08207.

Glubokovskikh, S. & Gurevich, B. 2015. Effect of micro-inhomogeneity on the effective stress coefficients and undrained bulk modulus of a poroelastic medium: a double spherical shell model. *Geophysical Prospecting* **63**, 656-668.

Guéguen, Y. & Schubnel, A. 2003. Elastic wave velocities and permeability of cracked rocks. *Tectonophysics* **370**, 163-176.

Hangx, S.J.T., Spiers, C.J. & Peach, C.J. 2010. Creep of simulated reservoir sands and coupled chemical-mechanical effects of CO_2 injection. *Journal of Geophysical Research: Solid Earth* **115**, B09205.

Hofmann, R., Xu, X., Batzle, M., Prasad, M., Furre, A.-K. & Pillitteri, A. 2005. Effective pressure or what is the effect of pressure? *The Leading Edge* **24**, 1256-1260.

Holt, R.M., Brignoli, M. & Kenter, C.J. 2000. Core quality: quantification of coring-induced rock alteration. *International Journal of Rock Mechanics and Mining Sciences* **37**, 889-907.

Holt, R.M., Nes, O.-M. & Fjaer, E. 2005. In-situ stress dependence of wave velocities in reservoir and overburden rocks. *The Leading Edge* **24**, 1268-1274.
Holt, R.M. & Stenebråten, J.F. 2013. Controlled laboratory experiments to assess the geomechanical influence of subsurface injection and depletion processes on 4D seismic responses. *Geophysical Prospecting* **61**, 476-488.
Kachanov, M. 1993. Elastic Solids with Many Cracks and Related Problems. In: *Advances in Applied Mechanics*, Vol. 30 (eds. J.W. Hutchinson & T.Y. Wu), pp. 259-445. Elsevier, ISBN 0065-2156.
Karner, S.L., Chester, F.M., Kronenberg, A.K. & Chester, J.S. 2003. Subcritical compaction and yielding of granular quartz sand. *Tectonophysics* **377**, 357-381.
Li, L. & Fjær, E. 2012. Modeling of stress-dependent static and dynamic moduli of weak sandstones. *Journal of Geophysical Research: Solid Earth* **117**, B05206.
Ma, X. & Zoback, M.D. 2017. Laboratory experiments simulating poroelastic stress changes associated with depletion and injection in low-porosity sedimentary rocks. *Journal of Geophysical Research: Solid Earth*, 2478-2503.
Madonna, C., Almqvist, B.S.G. & Saenger, E.H. 2012. Digital rock physics: numerical prediction of pressure-dependent ultrasonic velocities using micro-CT imaging. *Geophysical Journal International* **189**, 1475-1482.
North, L., Best, A.I., Sothcott, J. & MacGregor, L. 2013. Laboratory determination of the full electrical resistivity tensor of heterogeneous carbonate rocks at elevated pressures. *Geophysical Prospecting* **61**, 458-470.
Prasad, M. & Manghnani, M.H. 1997. Effects of pore and differential pressure on compressional wave velocity and quality factor in Berea and Michigan sandstones. *Geophysics* **62**, 1163-1176.
Rathore, J.S., Fjaer, E., Holt, R.M. & Renlie, L. 1995. P- and S-wave anisotropy of a synthetic sandstone with controlled crack geometryl1. *Geophysical Prospecting* **43**, 711-728.
Team, R.D.C. 2016. *R: A language and environment for statistical computing.* R Foundation for Statistical Computing.
Terzaghi, K., Peck, R.B. & Mesri, G. 1996. *Soil Mechanics In Engineering Practice, 3rd Ed.* Wiley-Interscience.
Tillotson, P., Chapman, M., Best, A.I., Sothcott, J., McCann, C., Shangxu, W. & Li, X.-Y. 2011. Observations of fluid-dependent shear-wave splitting in synthetic porous rocks with aligned penny-shaped fractures. *Geophysical Prospecting* **59**, 111-119.
Tillotson, P., Chapman, M., Sothcott, J., Best, A.I. & Li, X.-Y. 2014. Pore fluid viscosity effects on P- and S-wave anisotropy in synthetic silica-cemented sandstone with aligned fractures. *Geophysical Prospecting* **62**, 1238-1252.
Tillotson, P., Sothcott, J., Best, A.I., Chapman, M. & Li, X.-Y. 2012. Experimental verification of the fracture density and shear-wave splitting relationship using synthetic silica cemented sandstones with a controlled fracture geometry. *Geophysical Prospecting* **60**, 516-525.
Todd, T. & Simmons, G. 1972. Effect of pore pressure on the velocity of compressional waves in low-porosity rocks. *Journal of Geophysical Research* **77**, 3731-3743.
Vernik, L. & Hamman, J. 2009. Stress sensitivity of sandstones and 4D applications. *The Leading Edge* **28**, 90-93.

Wang, X.Q., Schubnel, A., Fortin, J., David, E.C., Guéguen, Y. & Ge, H.K. 2012. High Vp/Vs ratio: Saturated cracks or anisotropy effects? *Geophysical Research Letters* **39**, L11307.

Wang, Z. 2002. Seismic anisotropy in sedimentary rocks, part 1: A single-plug laboratory method. *Geophysics* **67**, 1415-1422.

Wang, Z., Gelius, L.-J. & Kong, F.-N. 2009. Simultaneous core sample measurements of elastic properties and resistivity at reservoir conditions employing a modified triaxial cell – a feasibility study. *Geophysical Prospecting* **57**, 1009-1026.

Wong, T.-f., David, C. & Menendez, B. 2004. Mechanical compaction (chapter 2). In: *Mechanics of Fluid Saturated Rocks* (ed. Y.G.a.M. Boutéca), pp. 55-114. Academic Press.

Xu, X., Hofmann, R., Batzle, M. & Tshering, T. 2006. Influence of pore pressure on velocity in low-porosity sandstone: Implications for time-lapse feasibility and pore-pressure study. *Geophysical Prospecting* **54**, 565-573.

1 **Figures**

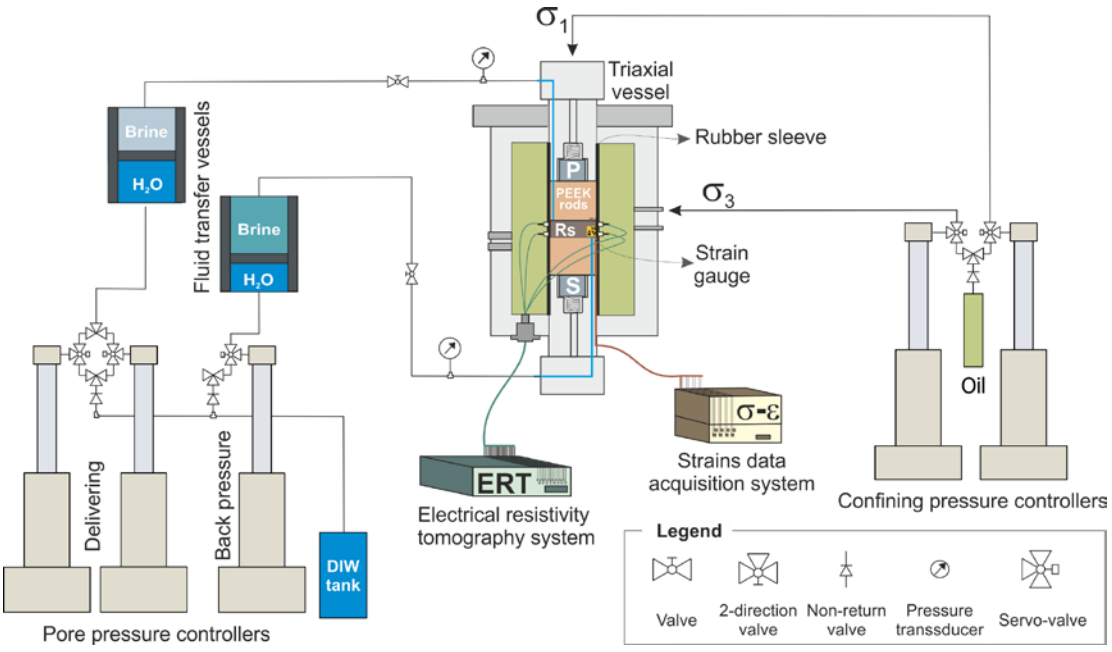

Figure 1. Experimental rig. P and S are the primary and secondary ultrasonic wave sensors, respectively, and Rs is the rock sample.

2

3

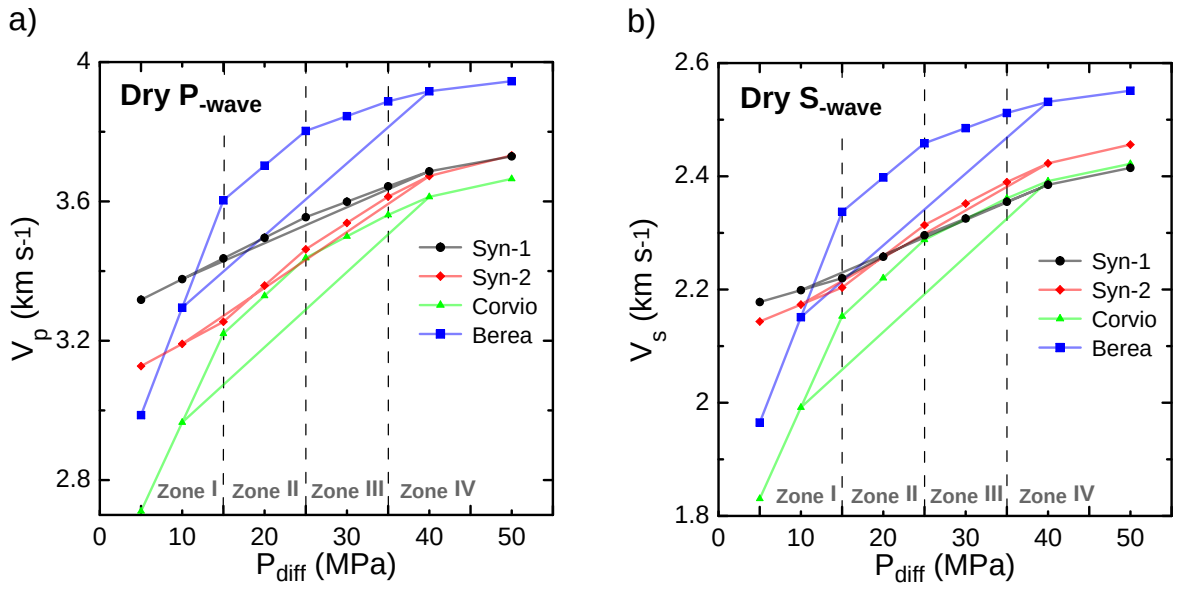

Figure 2. Ultrasonic P- and S-wave velocities (V_p and V_s) on dry samples. Preliminary evaluation of the elastic properties.

4

1

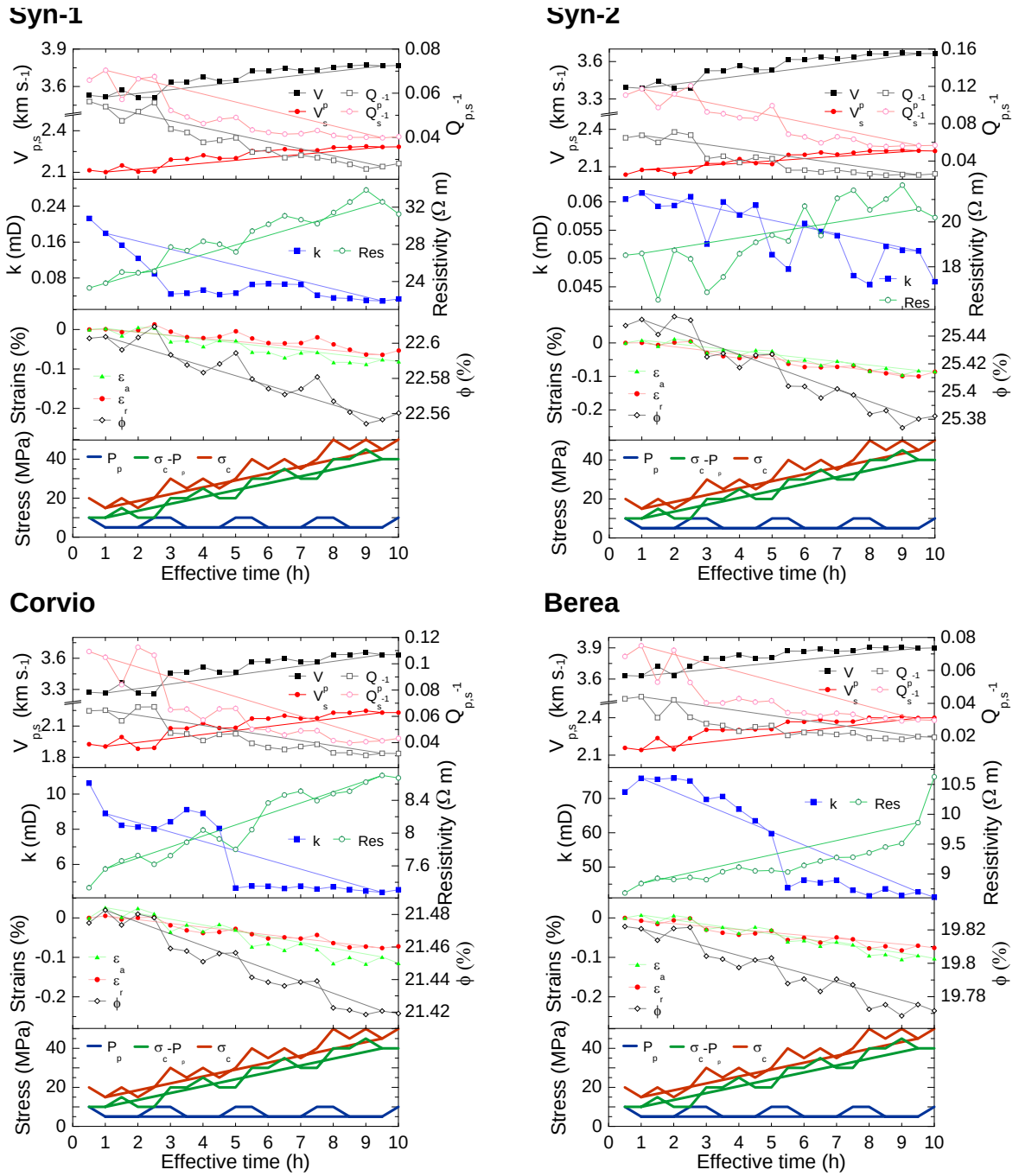

Figure 3. Ultrasonic P- and S-wave velocities (V_p, V_s) and attenuations (Q_p^{-1}, Q_s^{-1}), electrical resistivity, permeability (k), axial (ε_a) radial (ε_r) and derived porosity (ϕ) for different combinations of confining stress (σ_c) and pore pressure (P_p), on two synthetic (Syn-1 and Syn-2) and two natural (Corvio and Berea) sandstones.

2

3

a) b)

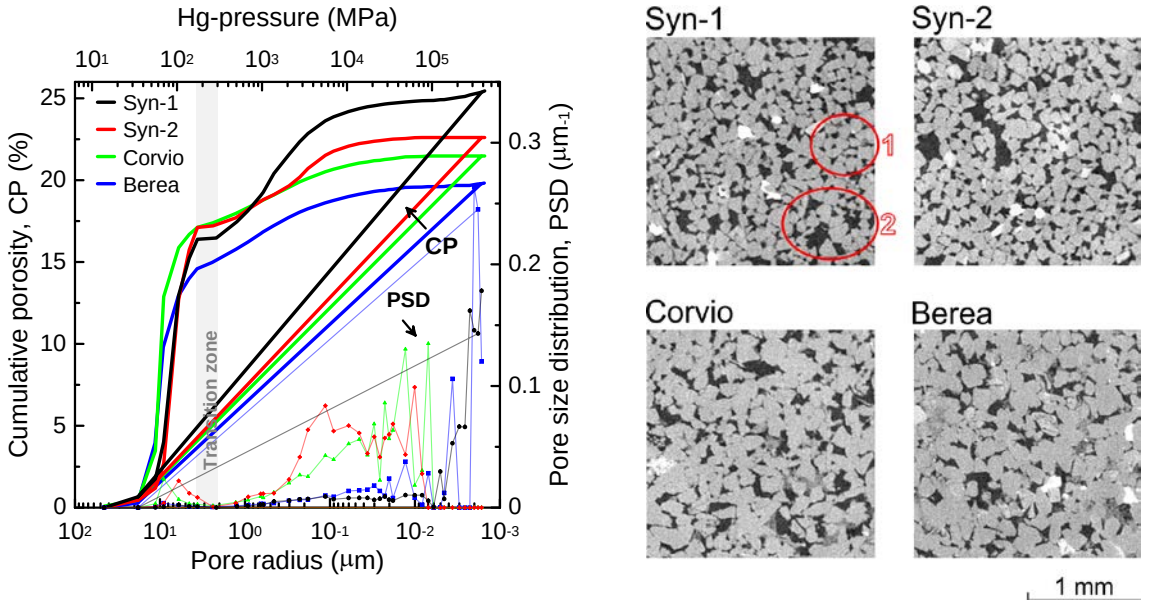

Figure 4. (a) Pore size distribution and (b) CT-scan images (orientated in the basal plane) of the four samples (1 and 2 circles highlight the presence of two different pore size families).

1

2

3

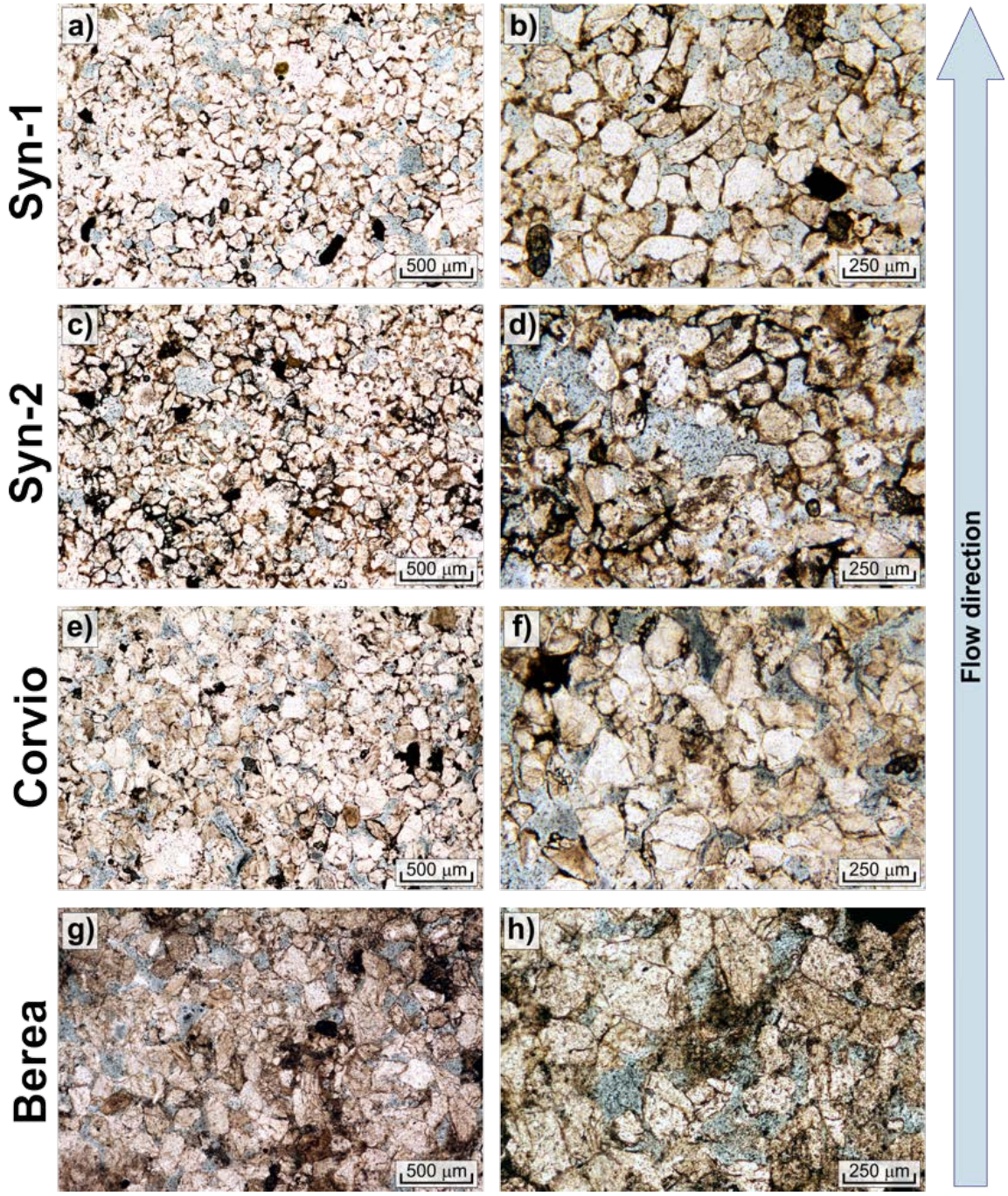

Figure 5. Textures assemblages in thin sections (oriented perpendicular to the basal plane of the samples) on the two synthetics (Syn-1, images a and b; Syn-2, c and d) and two natural (Corvio, images e and f; Berea, g and h) sandstones. Injected blue dye highlights the pore space . Photos taken under plane polarized light (PPL).

1

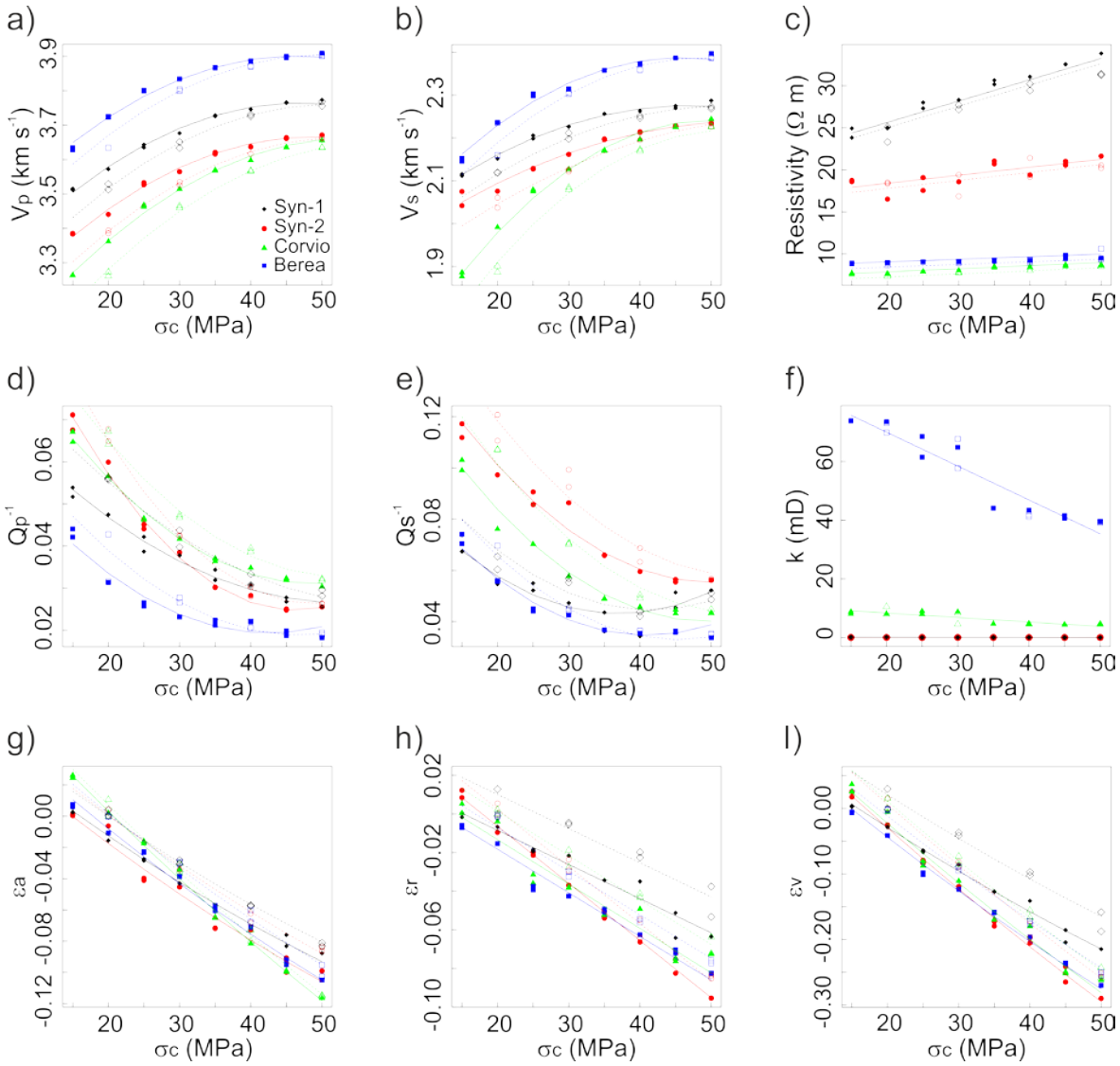

Figure 6. Ultrasonic P- and S-wave velocities (V_p, V_s) and attenuations (Q_p^{-1}, Q_s^{-1}), electrical resistivity, permeability (k) and axial (ε_a), radial (ε_r) and volumetric (ε_v) strains versus confining stress (σ_c), for synthetic sandstones Syn-1 and Syn-2, and Corvio and Berea samples. Empty circles and dash line for P_p=10 MPa; solids for P_p=5 MPa.

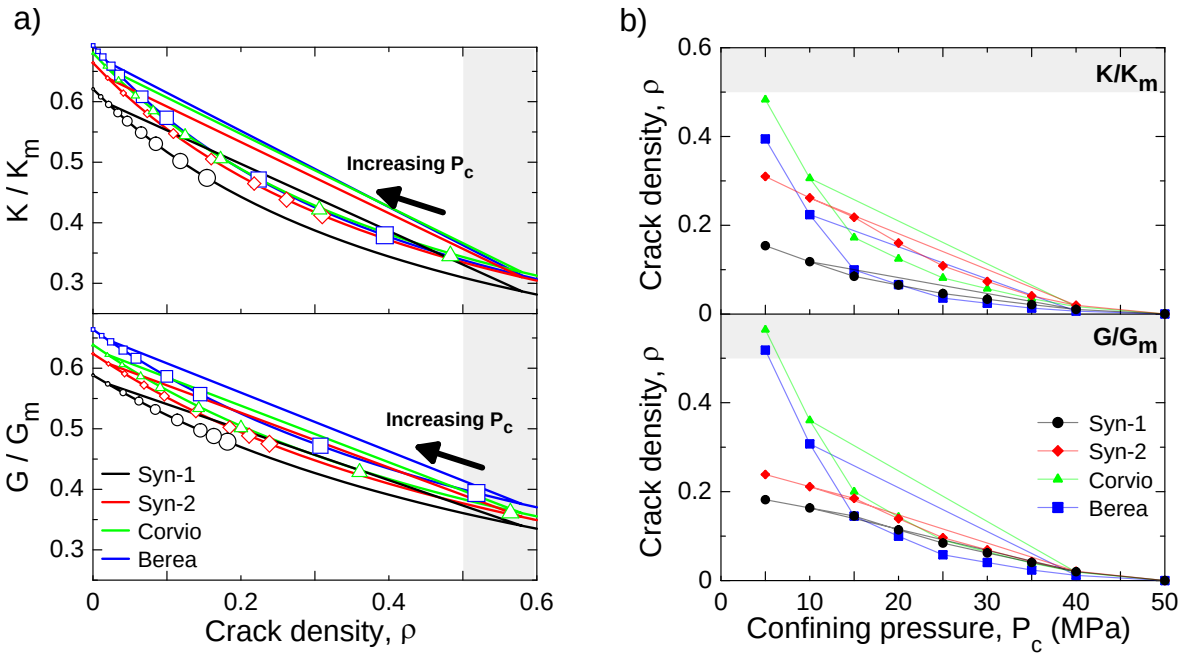

Figure 7. Estimations of the (a) effective bulk modulus ,K/K_m, and (b) shear modulus, G/G_m, for an ideal dry rock assuming spheroidal pores and penny-shaped cracks, versus crack density ρ (grey band, $\rho > 0.5$, represents the domain where the non-interactive scheme is no longer valid). One single curve per sample is plotted at their corresponding porosities. The points are estimations of the experimental data on the curves, with decreasing point size with increasing loading.

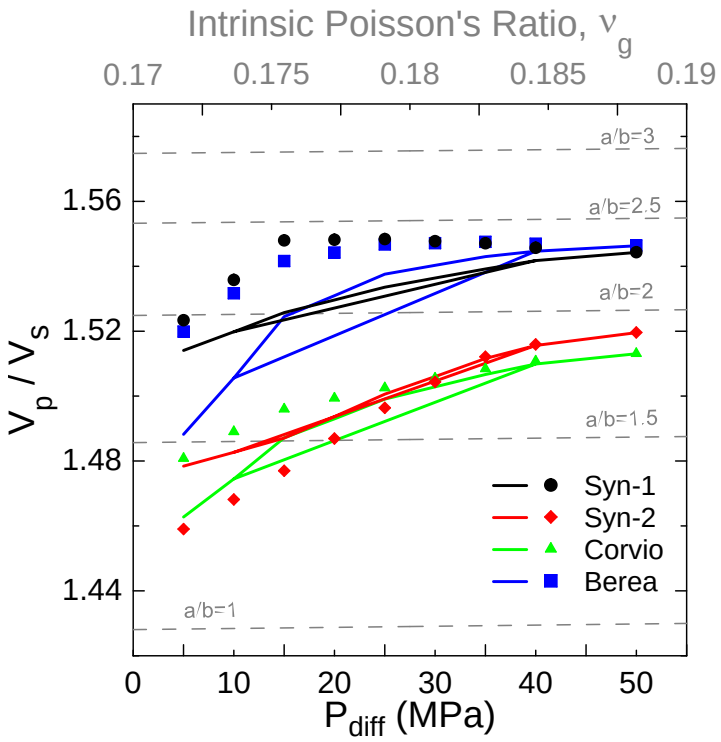

Figure 8. Granular cohesion model, based on Digby's model (Digby 1981). This model assumes a random packing of identical elastic spheres with bonding radius b and contact radius a. Dotted lines represent the V_p/V_s variation with the grains Poisson's ratio (ν_g) at fixed a/b ratios. The solid lines correspond to the V_p/V_s estimates for each sample derived from the "cracks and pores" model.

1

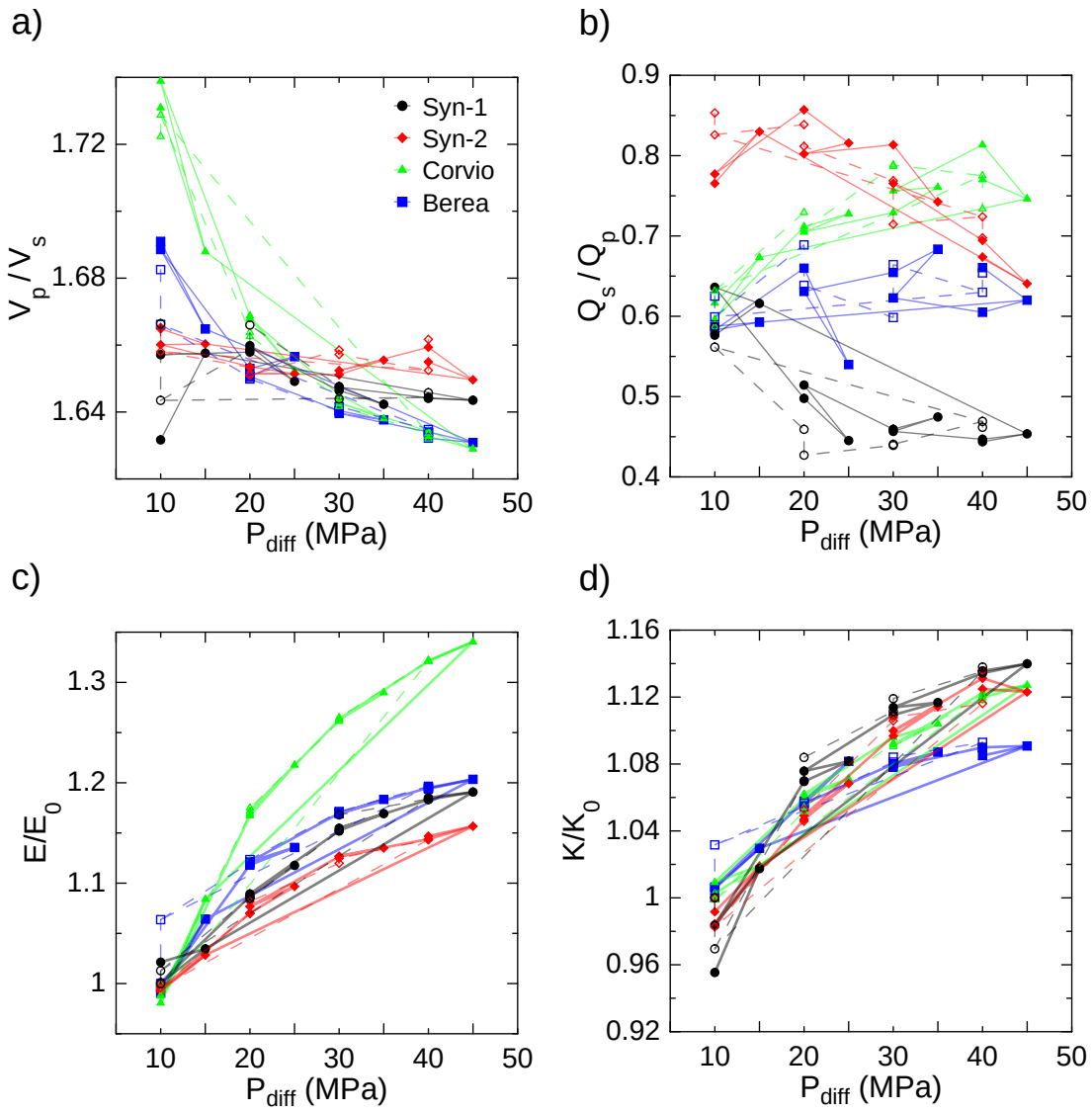

Figure 9. P- and S-wave velocity and attenuation ratios (V_p/V_s and Q_s/Q_p, respectively) and normalized Young's modulus (E) and bulk modulus (K) values versus differential pressure (P_{diff}), for the synthetic sandstones Syn-1 and Syn-2, and Corvio and Berea sandstones samples. Empty circles and dash line for P_p=10 MPa; solids for P_p=5 MPa.

1

2

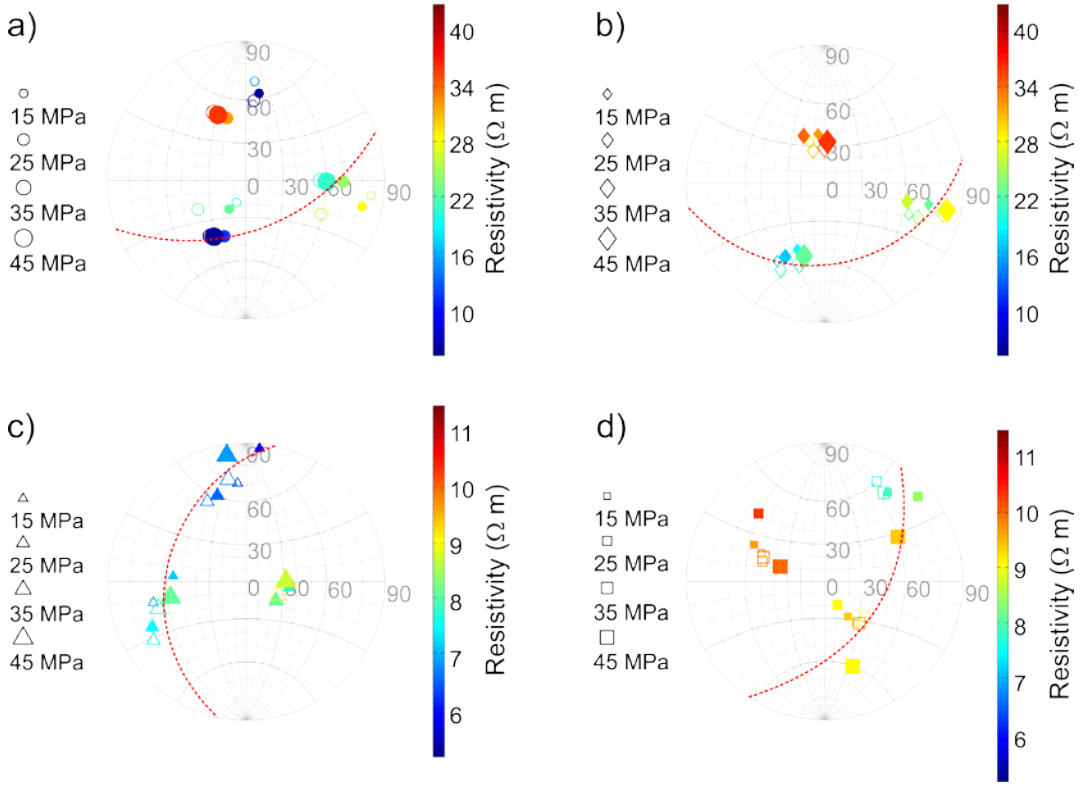

Figure 10. Stereographic plot illustrating the magnitude and orientation of the principle components of the tensorial anisotropy resistivity using the inversion scheme presented in North et al. (2013), for the synthetic sandstones Syn-1 (a) and Syn-2 (b), and Corvio (c) and Berea (d) sandstones samples at 15, 25, 35 and 45 MPa of differential pressure. Solid and empty symbols for measurements after variations in confining and pore pressure, respectively. Red dashed line marks the orthogonal plane of the maximum resistivity component.

1

2

3

TABLE CAPTIONS

Table 1. Physical properties of the synthetic (Syn-1 and Syn-2) and natural (Corvio and Berea) sandstones.

Table 2. R2 obtained for each based on multiple regression analysis

Table 3. Effective stress coefficients for the measured parameters

Table 4. Computed elastic constants for the crack-free matrix

Table 5. Initial values of the elastic parameters used in Figure 9.

FIGURE CAPTIONS

Figure 1. Experimental rig. P and S are the primary and secondary ultrasonic wave sensors, respectively, and Rs is the rock sample.

Figure 2. Ultrasonic P- and S-wave velocities (V_p and V_s) on dry samples. Preliminary evaluation of the elastic properties.

Figure 3. Ultrasonic P- and S-wave velocities (V_p, V_s) and attenuations (Q_p^{-1}, Q_s^{-1}), electrical resistivity, permeability (k), axial (ε_a) radial (ε_r) and derived porosity (ϕ) for different combinations of confining stress (σ_c) and pore pressure (P_p), on two synthetic (Syn-1 and Syn-2) and two natural (Corvio and Berea) sandstones.

Figure 4. (a) Pore size distribution and (b) CT-scan images of the four samples (1 and 2 circles highlight the presence of two different pore size families).

Figure 5. Textures assemblages in thin sections (oriented perpendicular to the basal plane of the samples) on the two synthetics (Syn-1, images a and b; Syn-2, c and d) and two natural (Corvio, images e and f; Berea, g and h) sandstones. Injected blue dye highlights the pore space . Photos taken under plane polarized light (PPL).

Figure 6. Ultrasonic P- and S-wave velocities (V_p, V_s) and attenuations (Q_p^{-1}, Q_s^{-1}), electrical resistivity, permeability (k) and axial (ε_a), radial (ε_r) and volumetric (ε_v) strains versus confining stress (σ_c), for synthetic sandstones Syn-1 and Syn-2, and Corvio and Berea samples. Empty circles and dash line for P_p=10 MPa; solids for P_p=5 MPa.

Figure 7. Estimations of the (a) effective bulk modulus ,K/K_m, and (b) shear modulus, G/G_m, for an ideal dry rock assuming spheroidal pores and penny-shaped cracks, versus crack density ρ (grey band, $\rho > 0.5$, represents the domain where the non-interactive scheme is no longer valid). One single curve per sample is plotted at

their corresponding porosities. The points are estimations of the experimental data on the curves, with decreasing point size with increasing loading.

Figure 8. Granular cohesion model, based on Digby's model (Digby 1981). This model assumes a random packing of identical elastic spheres with bonding radius b and contact radius a. Dotted lines represent the V_p/V_s variation with the grains Poisson's ratio (ν_g) at fixed a/b ratios. The solid lines correspond to the V_p/V_s estimates for each sample derived from the "cracks and pores" model.

Figure 9. P- and S-wave velocity and attenuation ratios (V_p/V_s and Q_s/Q_p, respectively) and normalized Young's modulus (E) and bulk modulus (K) values versus differential pressure (P_{diff}), for the synthetic sandstones Syn-1 and Syn-2, and Corvio and Berea sandstones samples. Empty circles and dash line for P_p=10 MPa; solids for P_p=5 MPa.

Figure 10. Stereographic plot illustrating the magnitude and orientation of the principle components of the tensorial anisotropy resistivity using the inversion scheme presented in North et al. (2013), for the synthetic sandstones Syn-1 (a) and Syn-2 (b), and Corvio (c) and Berea (d) sandstones samples at 15, 25, 35 and 45 MPa of differential pressure. Solid and empty symbols for measurements after variations in confining and pore pressure, respectively. Red dashed line marks the orthogonal plane of the maximum resistivity component.